The Effect of Gurney Flap Height on Vortex Shedding Modes Behind Symmetric Airfoils

Daniel R. Troolin[1], Ellen K. Longmire[2], Wing T. Lai[3]

1: TSI Incorporated, St. Paul, USA, dan.troolin@tsi.com
2: University of Minnesota, Minneapolis, USA, ellen@aem.umn.edu
3: TSI Incorporated, St. Paul, USA, wlai@tsi.com

Abstract A NACA 0015 airfoil with and without Gurney flaps (a small tab 1% to 4% of the airfoil chord that protrudes 90° to the chord at the trailing edge) was studied in a wind tunnel with $Re_c = 2.0 \times 10^5$ in order to examine the evolving flow structure of the wake through time-resolved PIV and hot-film anemometry frequency measurements. Multiple vortex shedding modes were observed and related to the flap height and angle of attack. Previous studies have shown the Gurney flap to increase the lift coefficient through an increase in circulation around the airfoil. This study examines the vortex shedding interactions that make this possible, and also shows that the ratio between the two dominant shedding modes is approximately 0.8 for both the 2% and 4% flap cases.

1. Introduction

The Gurney flap is a small tab approximately 1% to 4% of the airfoil chord in length that protrudes 90° to the chord at the trailing edge that is used to achieve higher lift. Daniel Gurney, for whom the flap is named, originally used it on a race car in 1971. Liebeck (1978) first studied the flap at length, and proposed the existence of counter-rotating vortices downstream of the flap. Wadcock (1987) performed wind tunnel tests at a Reynolds Number of 1.64×10^6 on a baseline NACA 4412 airfoil that showed a significant increase in the lift coefficient, shifting the lift curve up by 0.3 for a Gurney flap of 1.25% of the chord length, and providing a greater maximum lift. There was no appreciable increase in drag until the Gurney flap was extended beyond about 2% of the airfoil chord length, at which point the flap extended beyond the boundary layer thickness.

Jeffrey et al. (2000) studied the flap through surface pressure, LDA measurements, and flow visualization. The time-averaged velocity fields revealed a pair of counter-rotating vortices downstream of the flap, and spectra from the LDA measurements and smoke visualizations documented the presence of a Kármán vortex street. Two possible causes were postulated for the increase in lift caused by the flap: periodic vortex shedding downstream of the flap served to increase the trailing-edge suction of the airfoil, and the deceleration of the flow directly upstream of the flap contributed to a pressure difference acting across the trailing-edge. Time- and phase-averaged PIV analysis by Solovitz and Eaton (2004a and b) provided additional data on the flow pattern around static and dynamically-actuated Gurney flaps.

Previous studies (Troolin et al., 2006) conducted at $Re = 2.0 \times 10^5$ identified two dominant shedding modes in the region downstream of the Gurney flap. The primary mode resembles the common Kármán vortex street located downstream of bluff bodies. This shedding mode has a strong periodicity and contributes the strongest peak to the frequency spectra measured downstream of the airfoil. The secondary shedding mode results from fluid in the cavity upstream of the flap that is intermittently expunged into the downstream wake. The secondary shedding occurs less frequently and less periodically than the primary shedding; however a peak in the frequency spectra can be seen that corresponds to this shedding mode.

This study examines the effects of Gurney flap height on the vortex shedding and overall wake

structure behind a NACA 0015 airfoil through hot film anemometry, and time-resolved particle image velocimetry (TRPIV). TRPIV allows investigation of spatial and temporal details of flow patterns that are not easily observed or quantified by other measurement techniques. In this case, TRPIV is used to broaden the understanding of the interaction between the two shedding modes. Several types of vortex interaction, which occur due to the non-phase-locked nature of the shedding modes, are analyzed. The results are interpreted in terms of the known lift increment.

2. Experimental Setup

Experiments were performed in the blower driven open-return wind tunnel at the University of Minnesota Department of Aerospace Engineering. The tunnel cross-section was 0.6 m × 0.6 m and maintained a freestream turbulence intensity of less than 0.25%. The span (b) of the airfoil test sections was 304.8 mm; the chord length (c) was 190.5 mm, which gave an aspect ratio of A = 1.6. The airfoils and flap attachments were fabricated in a rapid-prototype machine at the University of Minnesota Department of Aerospace Engineering and Mechanics. The airfoil was mounted to a flat, circular plate and then to a sting, which entered the tunnel from the side so that it was horizontal and perpendicular to the freestream flow direction. The sting was capable of rotation, so that various angles of attack could be set with an accuracy of approximately 0.2°.

Three Gurney flap configurations were tested, with the length of the Gurney flap (h) measured relative to the total chord length of the airfoil from the tip of the flap to the chordline of the airfoil at the trailing edge: 1%, 2%, and 4%. In addition to the flapped airfoils, "closed" flap configurations (4% and 2%) were also tested (Fig. 1), in which the upstream cavity of the Gurney flap from the tip to the point 0.30c from the trailing edge on the pressure side of the airfoil, was filled in. This arrangement made it possible to determine the direct influence of the upstream recirculation region on the downstream wake. The control configuration consisted of a NACA 0015 symmetric airfoil with no flap; the wake characteristics of the airfoil without the flap are detailed in the paper by Troolin et al (2006). The hot-film anemometry and TRPIV data were conducted at a freestream velocity of U_∞ = 15.4 m/s. The Reynolds number based on chord length was 2.0 × 10^5. This freestream velocity was chosen to provide the largest possible Reynolds number while maintaining stability within the airfoil mounting apparatus.

Fig. 1 The closed flap configuration shown on the 4% flap.

Hot-film anemometry measurements were taken with a 50 μm diameter platinum-coated quartz substrate sensor with a sensing length of 1 mm. The measurement location was approximately 0.3c directly downstream of the trailing edge for the airfoil. Power spectra were obtained from runs taken for 2 minutes collected at a sampling rate of 2,000 Hz.

TRPIV is a simple extension of the standard PIV technique described well by Adrian (1991) whereby images are acquired at a faster rate. For this experiment, images were acquired at approximately the center of the wind tunnel span and center of the airfoil section, with the goal of minimizing 3-D effects occurring near the wingtip. Laser light sheets, formed from a pair of high-frequency pulsed Nd:YAG lasers, entered the tunnel from above, with the camera mounted on the side of the tunnel, as seen in Fig 2. The data from this configuration was inverted in the subsequent plots for purposes of comparison with previous work.

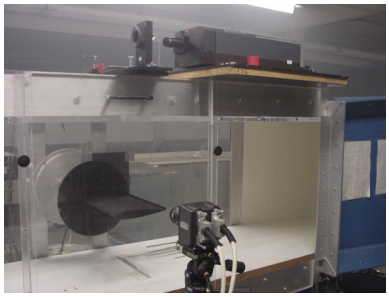

Fig. 2 Position of camera and laser in relation to the airfoil with Gurney flap.

In each flow case examined, sequences of 500 PIV fields were generated from images acquired at 2000 Hz (4000 fps) using a CMOS camera with 1000 x 1000 10-bit pixels. The time between frame-straddled laser pulses (Δt) was 35 μs, which allowed for a maximum particle displacement of 4 pixels at U_∞ = 15.4 m/s. Details on the high-speed lasers, light sheet formation, frame-straddling technique, camera, and seeding can be found in the paper by Troolin et al. (2006).

TSI software, INSIGHT3G, was used to process the data. The images were preconditioned by subtracting the minimum pixel intensity at every location across the sequence, diminishing the effect of constant sources of illumination such as background light, laser glare and noise. The vector fields were determined using a CDIC deformation algorithm described by Wereley and Gui (2001). This three-pass method resulted in an interrogation region of 16 by 16 pixels with 75% overlap, which corresponds to a resolution of slightly more than 2 mm square for the $(141\ \text{mm})^2$ field. The first two passes used a recursive grid to determine integer pixel displacement values. The final pass employed a four-corner deformation grid to improve measurement accuracy. This processing scheme yielded 98% or higher valid vectors in each field. The algorithm maintains a spatial displacement accuracy of approximately 0.1 pixels, so that the spatial displacement error in the following PIV data is on the order of 2.5% for a particle displacement of 4 pixels (= U_∞).

3. Results

Normalized streamwise velocity for the 4% flap at $\alpha = 8°$, averaged over 500 fields, is plotted in Fig. 3a. The white portion of the plot indicates the location of the flap. The gray region above the flap represents the area that was blocked from illumination by the light sheet; therefore there is no data in this region. The streamlines reveal a pair of counter-rotating vortices directly downstream of the flap. The streamlines downstream of the airfoil are deflected downwards from the horizontal, indicating the presence of circulation and lift due to the angle of attack and the asymmetry provided by the Gurney flap. A similar plot is shown in Fig. 3b for the 2% case. Of interest is the decreased boundary layer thickness on the suction side of the airfoil for the 4% case as compared to the 2% case, indicating that the longer flap serves to delay the separation point. This phenomenon of the Gurney flap delaying the separation point along the suction surface is consistent with the findings of Neuhart and Pendergraft (1988). Figure 3c shows the averaged streamwise velocity for the 4% closed flap configuration. There is a dramatic difference between this plot and Fig. 3a. The first point to note is the length of the average separated zone behind the closed flap, which is approximately twice as long in the streamwise direction as for the open flap case. In addition, the wake directly downstream of the closed flap is dominated by a negative vortex as indicated by the streamlines (here, negative is defined as clockwise). The length scale of the positive vortex is nearly the same in the streamwise direction, but approximately one-fifth the size in the normal direction. The average vortex pair downstream of the Gurney flap appears quite different, i.e. the vortex with positive rotation is strong and compact, while the negatively rotating

counterpart is relatively small. The direction of the streamlines for the closed flap case is also quite different than in the 4% open flap case. With the upstream cavity closed (Fig. 3c), the streamlines below the pressure surface of the airfoil are nearly horizontal, while on the suction surface, the streamlines are oriented approximately in the direction of slope of the upper airfoil surface. Contrast this with the 4% flap case (Fig. 3a), where the presence of the relatively large positive vortex in the downstream wake serves to entrain fluid from the pressure surface of the airfoil and limit the separation distance behind the flap. Downstream of the separation region, the streamlines reattach and deflect downward due to the higher velocity fluid entering from the suction surface. Note also that the streamlines in the 2% flap case (Fig. 3b) are angled less than in the 4% open flap case. These results are consistent with earlier measurements of lift coefficient that showed the highest value for the 4% open flap, followed by the 2% open flap and the 4% closed flap (C_L = 0.9, 0.77, and 0.73 respectively).

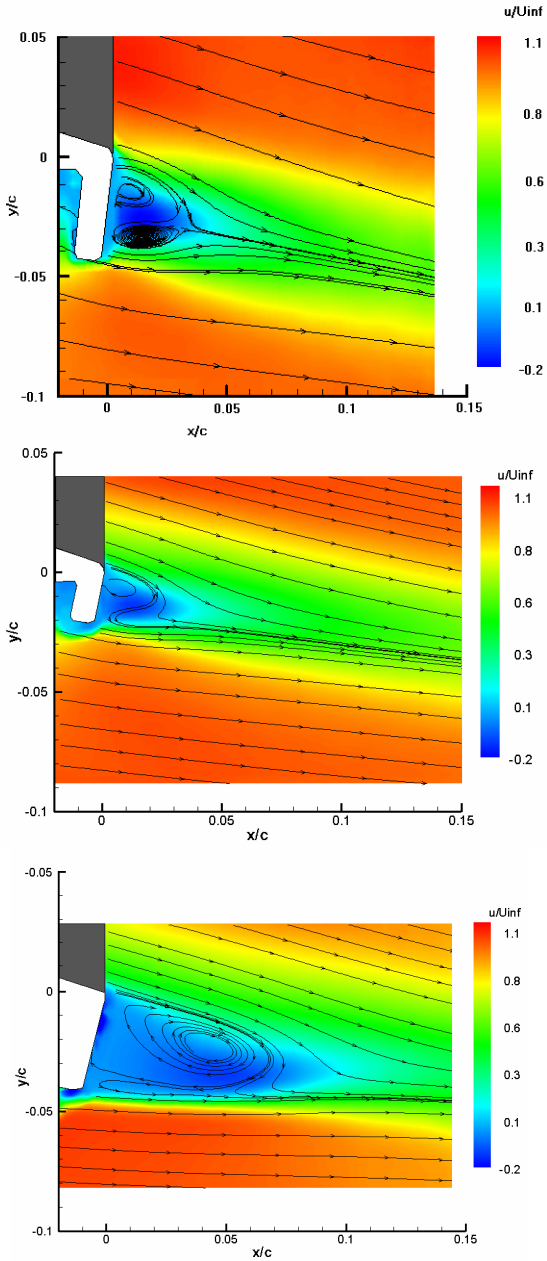

Fig. 3 Streamlines and time-averaged normalized streamwise velocity for a) 4% flap, b) 2% flap, c) 4% closed flap. Angle of attack = 8° in all cases.

Figure 4 displays two sequences of instantaneous normal velocity for the 4% flap configuration at $\alpha = 8°$. Red and blue indicate positive (upward) and negative (downward) normal velocity respectively. Each column represents a sequence in which the fluid from the cavity upstream of the flap is expunged into the downstream wake. This phenomenon is characterized by a burst of negative normal velocity (seen in blue) in the region just below the flap tip. The sequence on the left begins with a small region of negative normal velocity just upstream of the flap tip. As it progresses around the flap tip in the second frame, the region of positive normal velocity just downstream of the flap tip has begun to move downstream in the wake, so that it no longer occupies the region directly downstream of the flap. The negative burst then moves to the position downstream of the flap that was originally occupied by the positive normal velocity in the first frame. It then progresses downstream in the remaining three frames following the patch of positive normal velocity. In this case, a fairly smooth transition occurs from the upstream cavity to the downstream wake. The interaction between the two shedding modes (the Kármán vortex street downstream of the flap, and the secondary shedding mode resulting from fluid filling up the upstream cavity and then being expunged) is seamless and smooth, since the burst of downward normal velocity from the upstream cavity coincides with the downward normal velocity phase of the downstream shedding. Constructive interference takes place between the two shedding modes.

Contrast these events with those seen in the sequence on the right, in which the fluid begins to enter the wake while the downstream shedding is forming and releasing a region of positive normal velocity. Once again, the sequence begins with a patch of negative normal velocity (blue) forming directly upstream of the flap tip. Directly downstream, a region of positive normal velocity (red) is just beginning to form. The upstream downward motion continues over the next three frames, and does not begin to enter the downstream wake until the fifth frame. When it finally emerges and enters the downstream wake, the wake is characterized by smaller regions of upward and downward velocity, whose length scale is smaller (on the order of 1/3 to 1/2) than the length scale seen in the first sequence. The wake is much less organized, suggesting that the downward motion from the upstream cavity served to diminish the strength of the upflow immediately downstream of the flap. In this case, destructive interference occurs between the two shedding modes.

In general, the burst of negative normal velocity coming from the upstream cavity either serves to enhance the same-signed velocity in the downstream wake, or diminish the strength of the opposite-signed region of normal velocity. Both possibilities cause an instantaneous increase in the circulation around the airfoil that would not exist without the presence of the upstream shedding.

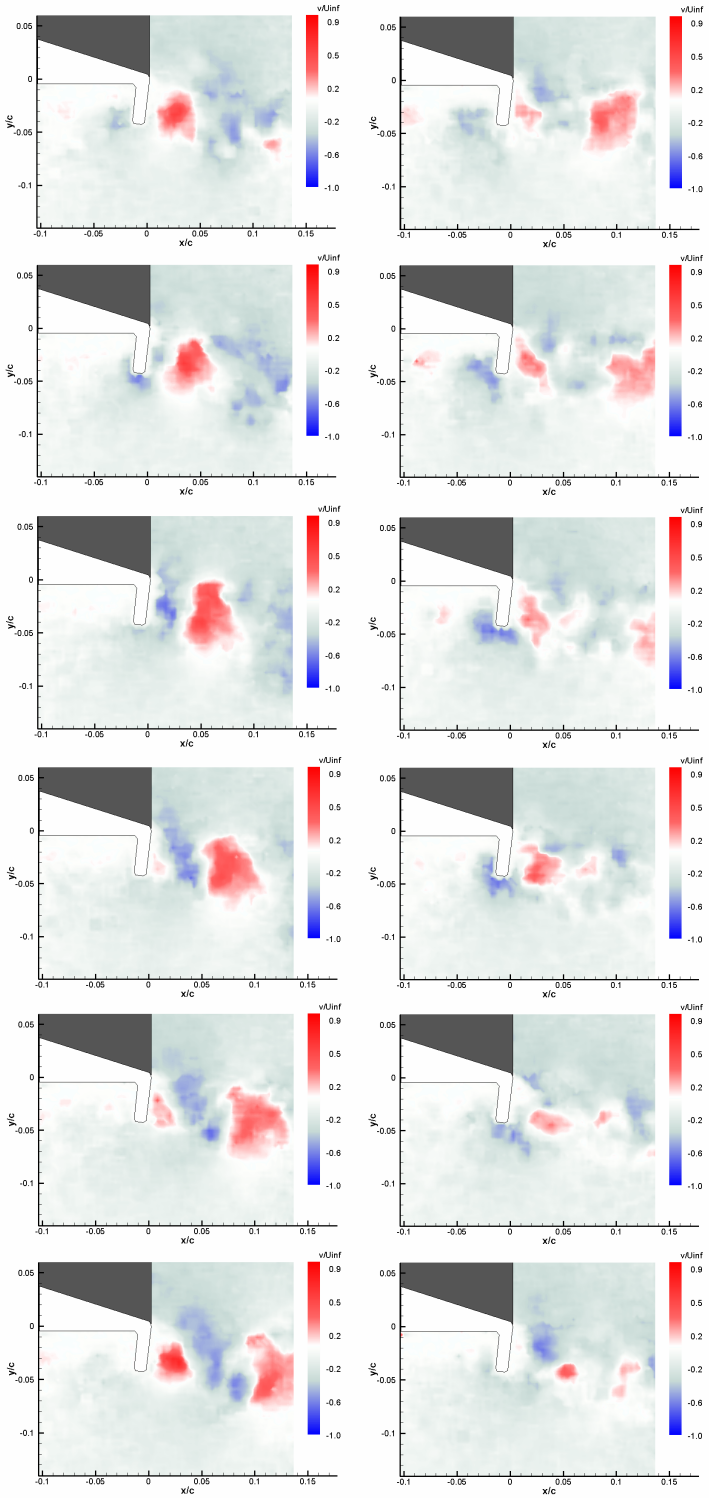

Fig. 4 Two top-to-bottom sequences of normalized normal velocity for the 4% flap case, shown in intervals of tU_∞/h = 0.91, $\alpha = 8°$. Left sequence shows a burst of negative normal velocity emerging from the upstream cavity of the flap and coinciding with a downflow occurring in the primary shedding. Right sequence shows a downward burst that interacts with an upflow.

The top two figures shown in Fig. 5 shows two normalized 2D swirl plots (to identify vortex cores) corresponding to the fourth row in Fig. 4. Since the 2D swirl is a positive scalar, the values

have been given a sign based upon the sign of the vorticity at that location. The bottom two figures represent the normalized vorticity for the same plots. These frames coincide with the time where the burst of negative normal velocity enters the wake in the left-hand column. At this instant, the wake is characterized by alternating evenly-spaced regions of positive and negative swirl. In contrast, in the right-hand plot, smaller swirling zones are spread out in two rows, one above with negative vorticity, and the other below with positive vorticity. The vorticity plots (bottom) also show a great variation between the two, with the plot on the left showing a clear vortex street pattern, while the plot on the right is more characteristic of two opposite-signed shear layers.

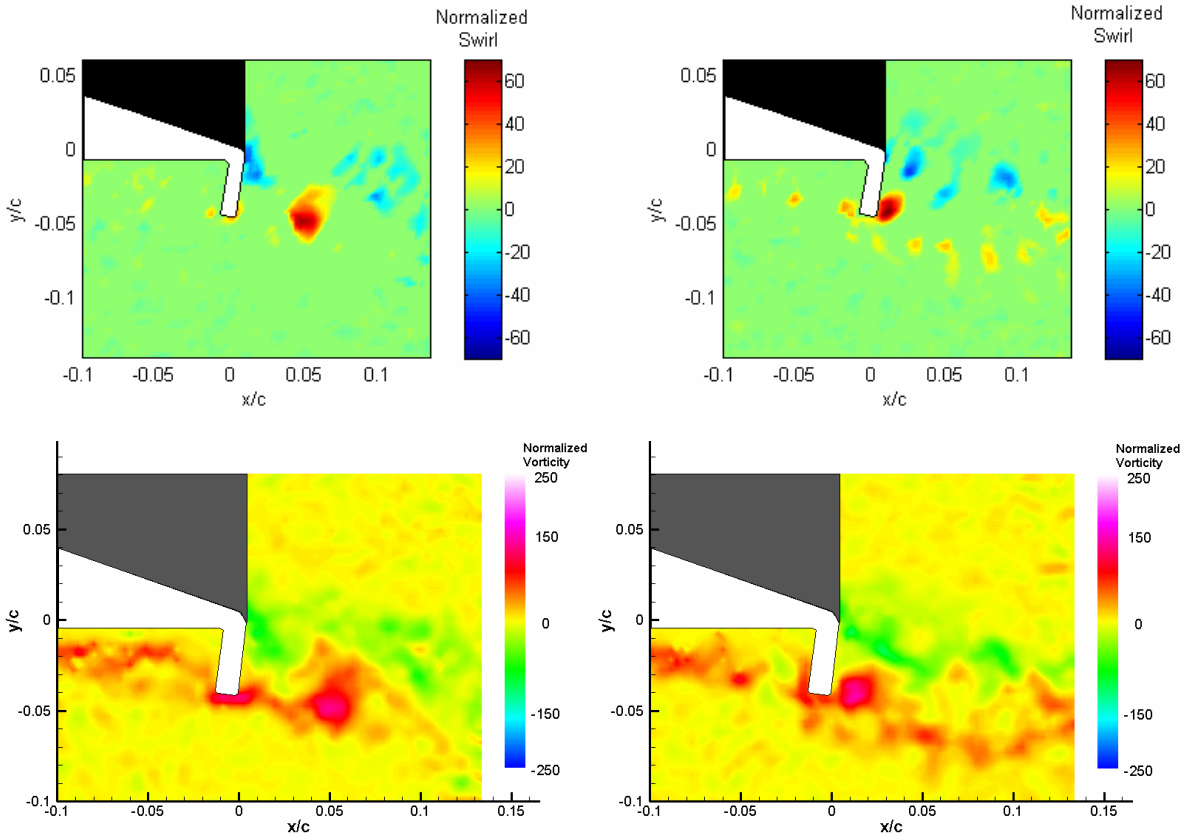

Fig. 5 Signed 2D swirl field (normalized, above) for 4th row from top from previous figure and corresponding vorticity fields (below).

Figure 6 displays sequences of normal velocity for the 2% flap configuration at $\alpha = 8°$. Similar phenomena to the 4% sequence are seen, though with coherent structures of smaller length scale, as would be expected from the smaller flap height. The column on the left shows an example of the constructive interference between the two shedding modes. In the first plot, a small region of downflow is directly below the flap tip. In the second frame, it begins to move into the wake downstream of the flap, adding to the downward velocity from the primary shedding sequence. The downflow is intensified, and it continues downstream in the subsequent frames. The column on the right exhibits a case of destructive interference, where the first plot also shows a downflow region below the flap tip. This time it attempts to emerge into the downstream wake during the formation of upward velocity in the primary shedding mode. The entrance of the upstream fluid to the wake is delayed until the fourth frame, where it then proceeds downstream. Notice the stark difference between the two columns, in that the presence of positive normal velocity (red) is very much diminished in the right-hand column.

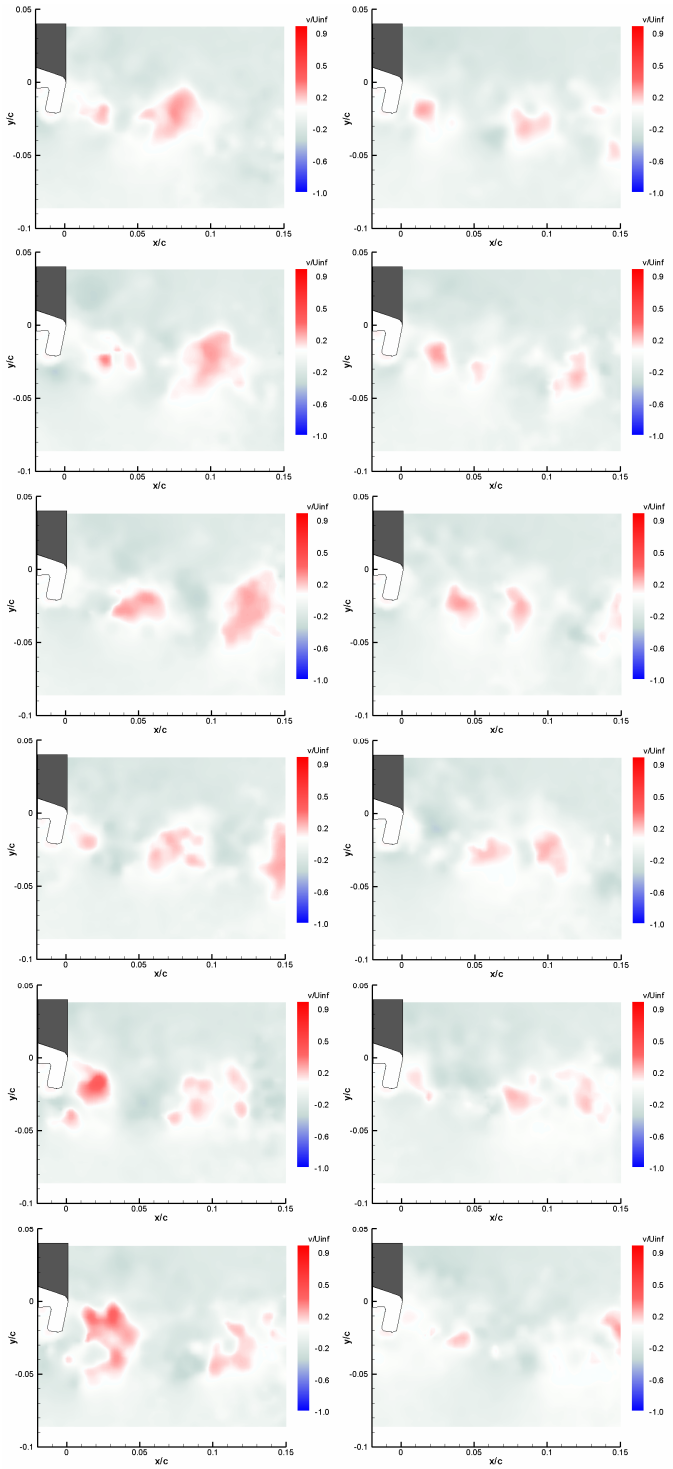

Fig. 6 Two top-to-bottom sequences of normal velocity for the 2% flap case, shown in intervals of $tU_\infty/h = 1.7$, $\alpha = 8°$. Left sequence shows a burst of negative normal velocity emerging from the upstream cavity of the flap and coinciding with a downflow occurring in the primary shedding. Right sequence shows a downward burst that interacts with an upflow.

Figure 7 shows the normalized 2D swirl and vorticity fields for the 2% flap case. Although it is difficult to discern significant differences in the distributions of vortex cores, the vorticity fields appear different in the following way: in the left-hand case of 'constructive interference', the

positive vorticity is distributed in larger scale blobs, while in the right-hand case of 'destructive interference', the vorticity is distributed in a more continuous shear layer. This is similar to the trend seen in Fig 5 for the 4% flap.

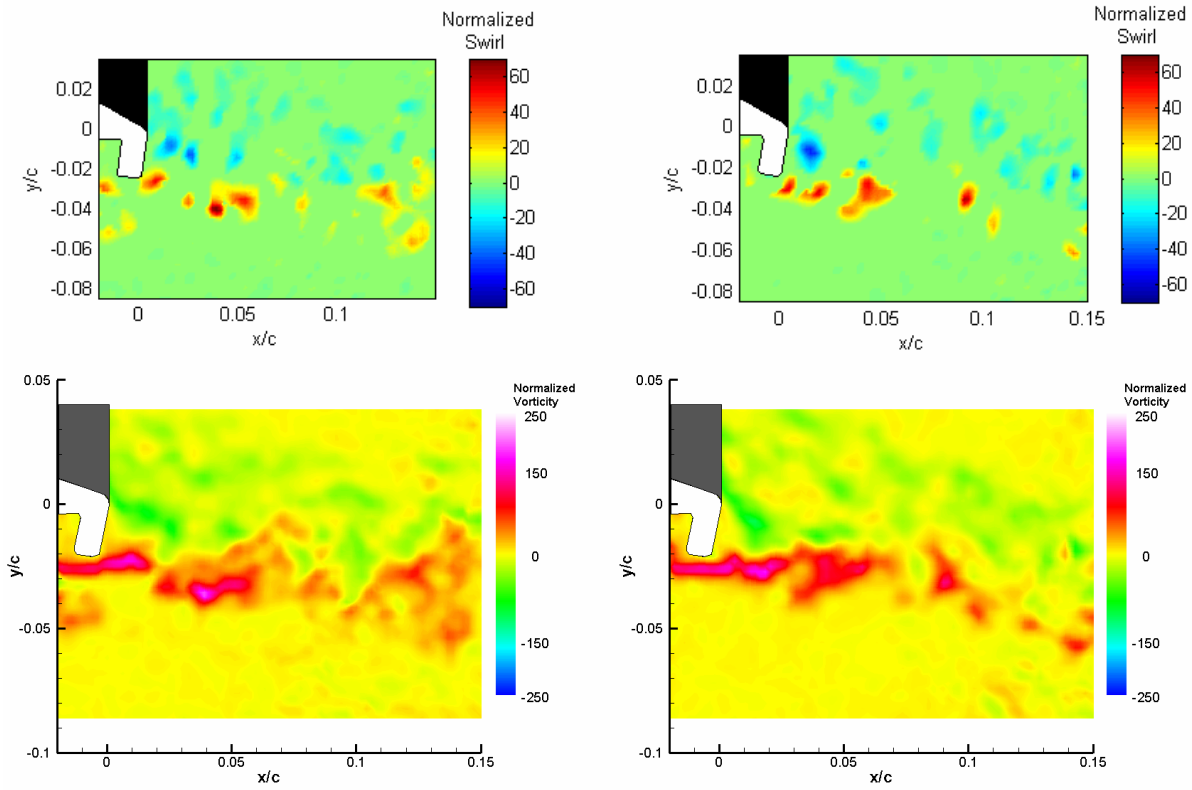

Fig. 7 Signed 2D swirl field (normalized, above) for 4th row from top from previous figure, and corresponding vorticity fields (below).

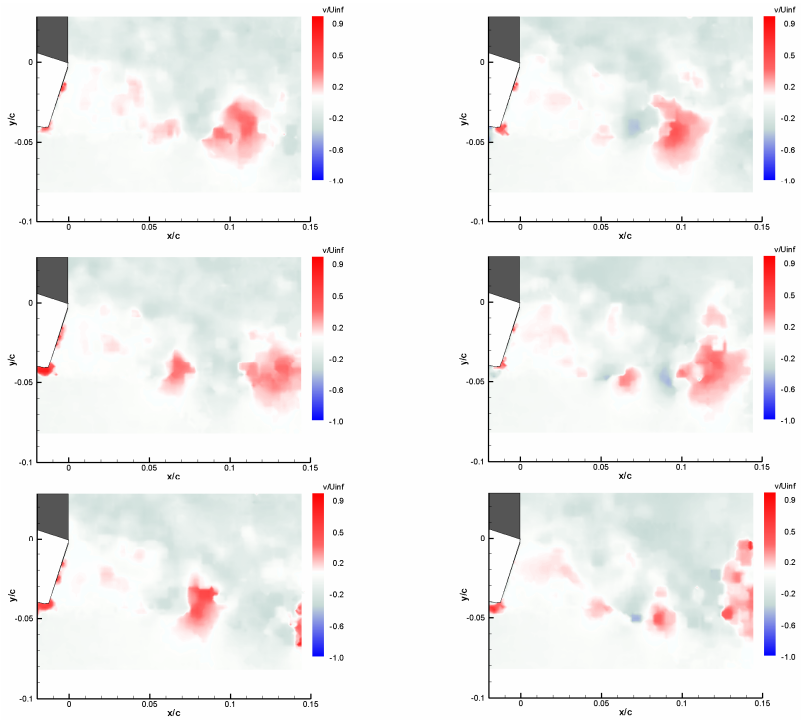

Fig. 8 One sequence of normal velocity for the 4% closed flap case, shown in intervals of $tU_\infty/h = 0.91$, $\alpha = 8°$. The order is from top to bottom; the bottom plot in the left column is followed by the top plot in the right column.

Figure 8 depicts a typical shedding cycle for the 4% closed flap case. Once again, the normal velocity component is plotted. A region of general disorder occurs directly downstream of the flap which is characterized by low magnitude, but primarily upward velocity. Coherent patches of significant positive and negative normal velocity zones do not manifest themselves until greater than 0.05c downstream of the flap. The central portion of the wake has weaker negative or downward velocity zones (blue) than the 4% flap case (Fig. 4), consistent with the diminished lift value for this case. (However, the reduced downward velocities in the lower portion of the wake is likely a stronger factor).

Power spectra obtained through hot-film anemometry for the 4% flap case for $\alpha = 0°$, 4°, and 8° are displayed in Fig. 9. As the angle of attack is increased, the dominant frequency decreases in magnitude, but increases in energy. This dominant peak corresponds to the Kármán shedding mode. Also visible in the plots are harmonics to the right of each dominant peak. Of interest in this study is the secondary peak at a slightly lower frequency that begins to form and increase in magnitude as the angle of attack increases. It is most easily seen as the hump located just to the left of the highest peak in the $\alpha = 8°$ and $\alpha = 4°$ cases. The ratio between the first and second shedding modes for the cases where $\alpha = 8°$ and 4°, are 0.78 and 0.82 respectively.

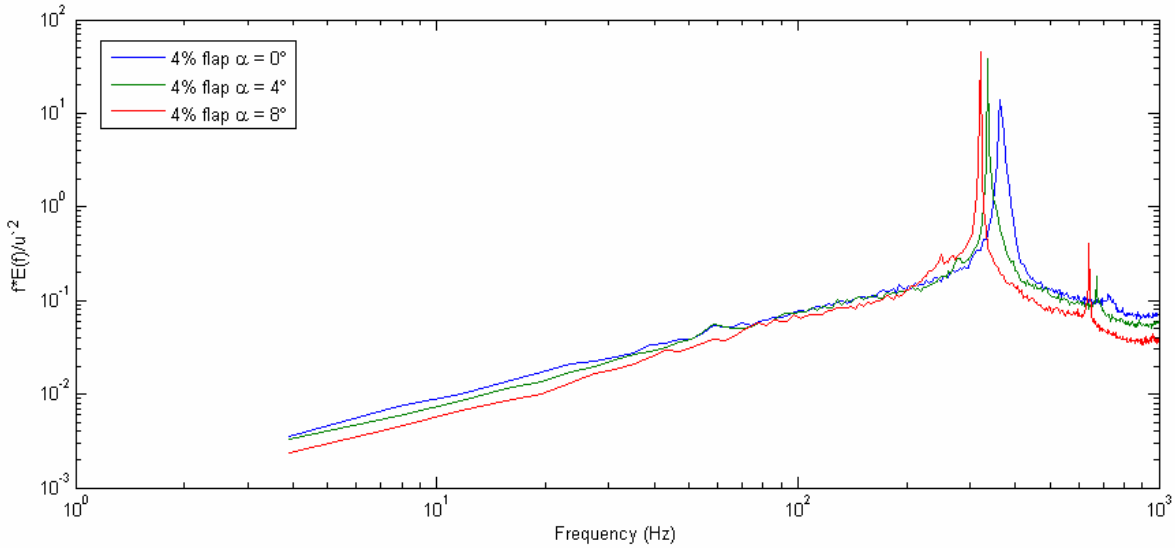

Fig. 9 Frequency spectra for the 4% flap at $\alpha = 0°$, 4°, and 8°.

Figure 10 displays the corresponding spectra for the 2% flap case. In this case, the spectra reveal additional peaks at lower frequencies, especially when $\alpha = 0°$. Nevertheless, the primary peak is still easily discernible for all three angles. The secondary shedding peak is clear for $\alpha = 8°$, but not for the lower angles. The ratio between the two dominant frequencies for the $\alpha = 8°$ case is 0.81 which is nearly identical to the value found for the 4% flap. Thus, this ratio may be independent of flap height for configurations that support coherent shedding. Spectra were also examined for the 1% Gurney flap. Many additional peaks were present, and primary or secondary peaks were difficult to discern.

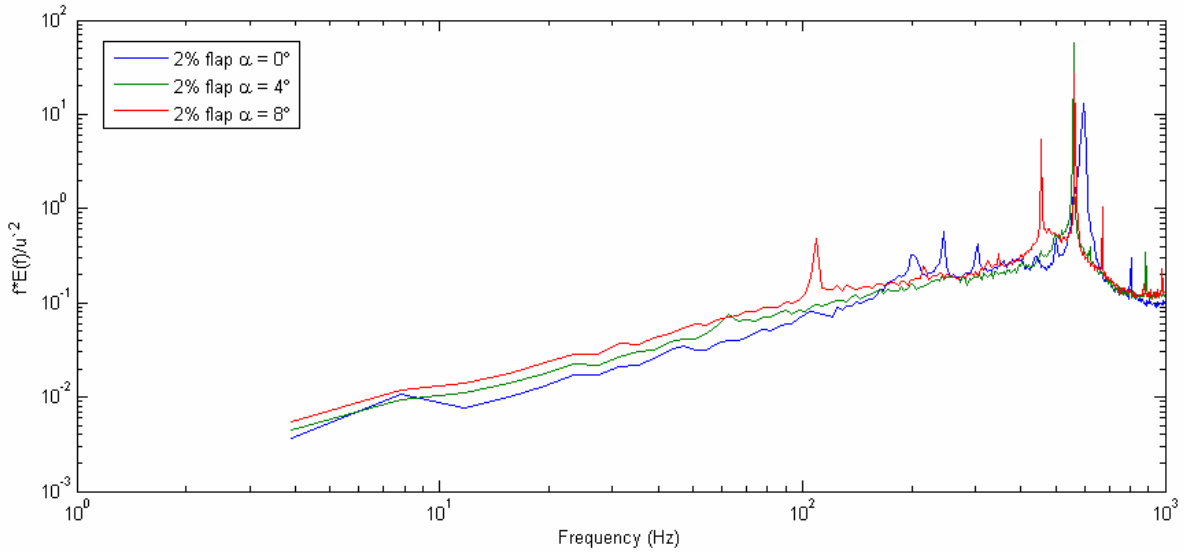

Fig. 10 Frequency spectra for the 2% flap at α = 0°, 4°, and 8°.

4. Conclusions

The TRPIV velocity fields and spectra from hot-film measurements revealed the nature of the upstream and downstream shedding modes, their interactions, and their dependence upon the flap height. Two shedding modes of different frequency interact downstream of the flap to generate constructive or destructive interference depending on the phases during which they merge. In all cases, these interactions served to increase the negative normal velocity in the airfoil wake, and thus the circulation and lift, as compared to the closed flap case.

The different flap heights displayed very similar wake and shedding interference patterns, with the coherent structures in each scaling approximately with the height of the flap. For example, Strouhal numbers $St = hf/U$ associated with the primary and secondary shedding modes at α = 8° were (0.17, 0.14) and (0.16, 0.13) for the 4% and 2% flaps respectively. Also, the ratio of primary to secondary shedding modes was found to be nearly constant at approximately 0.8 for the 4% and 2% flap configurations. Thus, these preliminary results suggest that perhaps the shedding mode ratio is independent of the Gurney flap height, as long as coherent shedding modes exist.

Future work will include a more detailed analysis of the closed flap configuration for varying sizes of Gurney flap and a more accurate determination of the boundary layer thickness on the suction surface of the airfoil. In addition, the vortex interactions will be analyzed for different Reynolds numbers, hence different boundary layer thicknesses, to determine whether there is a significant effect on the vortex shedding.

5. Acknowledgements

The authors thank the University of Minnesota Aerospace Engineering & Mechanics Department for the use of the facilities and for fabrication of the airfoil test sections.

6. References

Adrian R (1991) Particle-Imaging Techniques for Experimental Fluid Mechanics. University of Illinois, Annual Review Fluid Mechanics, Vol. 23, pp 261-304.

Blake W (1986) Mechanics of Flow-Induced Sound and Vibration Vol. II, Academic Press, Inc., pp. 756-782.
Jeffrey D; Zhang X; Hurst D (2000) Aerodynamics of Gurney Flaps on a Single-Element High-Lift Wing, Journal of Aircraft, Vol. 37. No. 2, pp. 295-301.
Liebeck R (1978) Design of subsonic airfoils for high lift. Journal of Aircraft 15(9), pp. 547-61.
Neuhart D; Pendergraft O (1988) A water tunnel study of Gurney flaps. NASA TM 4071.
Solovitz S; Eaton J (2004) Spanwise Response Variation for Partial-Span Gurney-Type Flaps, AIAA Journal, Vol. 42, No. 8, pp. 1640-1643.
Solovitz S; Eaton J (2004) Dynamic Flow Response Due to Motion of Partial-Span Gurney-Type Flaps, AIAA Journal, Vol. 42, No. 9, pp. 1729-1736.
Troolin D; Longmire E; Lai W (2006) Time resolved PIV analysis of flow over a NACA 0015 airfoil with Gurney flap, Experiments in Fluids, published online, in press.
Wadcock A (1987) Investigations of low-speed turbulent separated flow around airfoils. NASA CR 177450.
Wereley S; Gui L (2001) PIV measurement in a four-roll-mill flow with a central difference image correction (CDIC) method, 4th International Symposium on Particle Image Velocimetry, Göttingen, Germany, September 17.